The Astrophysical Journal, 893:46 (14pp), 2020 April 10 https://doi.org/10.3847/1538-4357/ab7a18

The Fourth Fermi-GBM Gamma-Ray Burst Catalog: A Decade of Data

A. von Kienlin[1], C. A. Meegan[2], W. S. Paciesas[3], P. N. Bhat[2,4], E. Bissaldi[5,6], M. S. Briggs[2], E. Burns[7], W. H. Cleveland[3], M. H. Gibby[8], M. M. Giles[8], A. Goldstein[3], R. Hamburg[2,4], C. M. Hui[9], D. Kocevski[10], B. Mailyan[2], C. Malacaria[11,12], S. Poolakkil[2,4], R. D. Preece[4], O. J. Roberts[3], P. Veres[2], and C. A. Wilson-Hodge[9]
[1] Max-Planck-Institut für extraterrestrische Physik, Giessenbachstrasse 1, D-85748 Garching, Germany; azk@mpe.mpg.de
[2] Center for Space Plasma and Aeronomic Research, University of Alabama in Huntsville, 320 Sparkman Drive, Huntsville, AL 35899, USA
[3] Science and Technology Institute, Universities Space Research Association, 320 Sparkman Drive, Huntsville, AL 35805, USA
[4] Department of Space Science, University of Alabama in Huntsville, 320 Sparkman Drive, Huntsville, AL 35899, USA
[5] Dipartimento Interateneo di Fisica, Politecnico di Bari, Via E. Orabona 4, I-70125 Bari, Italy
[6] INFN—Sezione di Bari, Via E. Orabona 4, I-70125 Bari, Italy
[7] NASA Postdoctoral Program Fellow, Goddard Space Flight Center, Greenbelt, MD 20771, USA
[8] Jacobs Space Exploration Group, Huntsville, AL 35806, USA
[9] NASA Marshall Space Flight Center, Huntsville, AL 35812, USA
[10] Astrophysics Office, ST12, NASA/Marshall Space Flight Center, Huntsville, AL 35812, USA
[11] NASA Postdoctoral Program Fellow, Marshall Space Flight Center, NSSTC, 320 Sparkman Drive, Huntsville, AL 35805, USA
[12] Universities Space Research Association, NSSTC, 320 Sparkman Drive, Huntsville, AL 35805, USA
Received 2019 December 20; revised 2020 February 10; accepted 2020 February 24; published 2020 April 14

Abstract

We present the fourth in a series of catalogs of gamma-ray bursts (GRBs) observed with Fermi's Gamma-ray Burst Monitor (Fermi-GBM). It extends the six year catalog by four more years, now covering the 10 year time period from trigger enabling on 2008 July 12 to 2018 July 11. During this time period GBM triggered almost twice a day on transient events, 2356 of which we identified as cosmic GRBs. Additional trigger events were due to solar flare events, magnetar burst activities, and terrestrial gamma-ray flashes. The intention of the GBM GRB catalog series is to provide updated information to the community on the most important observables of the GBM-detected GRBs. For each GRB the location and main characteristics of the prompt emission, the duration, peak flux, and fluence are derived. The latter two quantities are calculated for the 50–300 keV energy band, where the maximum energy release of GRBs in the instrument reference system is observed and also for a broader energy band from 10–1000 keV, exploiting the full energy range of GBM's low-energy detectors. Furthermore, information is given on the settings of the triggering criteria and exceptional operational conditions during years 7 to 10 in the mission. This fourth catalog is an official product of the Fermi-GBM science team, and the data files containing the complete results are available from the High-Energy Astrophysics Science Archive Research Center.

Unified Astronomy Thesaurus concepts: Catalogs (205); Gamma-ray bursts (629)

Supporting material: machine-readable tables

1. Introduction

With the completion of the first decade of operation, Fermi-GBM has been in orbit longer than its predecessor experiment, the Burst and Transient Source Experiment (BATSE)[13] on board the Compton Gamma Ray Observatory (∼9 yr of operation). Despite its lower sensitivity and smaller detectors, the GBM instrument is capable of detecting almost the same number of gamma-ray bursts (GRBs; ∼240 GBM GRBs compared to ∼300 BATSE GRBs per year), mostly thanks to its advanced triggering system (Paciesas et al. 2012). Thus, it successfully continues to detect and coarsely locate GRBs over a wide field of view (FOV), and to provide broad spectral information in the hard X-ray and soft gamma-ray energy range (8 keV–40 MeV) where bursts emit most of their energy.

The Fermi-GBM science team releases catalogs on a regular basis that list the main characteristics of triggered bursts, compiling the data of several completed mission years. These have included the first two (first GBM GRB catalog, Paciesas et al. 2012), four (second, von Kienlin et al. 2014), and six (third, Bhat et al. 2016) mission years, which are now continued by the current 10 year catalog. The first two catalogs were accompanied by spectral catalogs, for the first two (Goldstein et al. 2012) and four (Gruber et al. 2014) mission years, which provide more detailed information on the spectral characteristics of nearly all GRBs, including the time-integrated fluence and peak flux spectra. These results are updated by the current 10 year spectral catalog (S. Poolakkil et al. 2020, in preparation). A time-resolved spectral analysis of the brightest 81 GRBs observed during the first four mission years is provided in the first time-resolved spectral catalog (Yu et al. 2016). It will be continued in a forthcoming catalog (E. Bissaldi et al. 2020, in preparation) presenting the time-resolved spectral analysis for the brightest GRBs of the first 10 years.

The GRB detection capabilities of GBM are augmented by Fermi's primary instrument, the Large Area Telescope (LAT), which overlaps and extends the GBM energy range (30 MeV–300 GeV), allowing observations over more than seven decades in energy. The second LAT GRB catalog (Ajello et al. 2019), which covers the first 10 years of operations, from 2008 to 2018 August 4, lists 176 GRBs jointly detected by LAT and GBM, emphasizing the great scientific merit of LAT in uncovering previously unknown characteristics of GRBs at high gamma-ray energies. Examples include the delayed onset and extended duration of the emission above 100 MeV and the observation of additional spectral components. We note that

[13] https://gammaray.nsstc.nasa.gov/batse/

Table 1
Trigger Statistics of the First 10 Mission Years, Subdivided into 2 Year Sections

Cat #	Year[a]	GRBs	SGRs	TGFs	SFs	Galactic	CPs	Other	Sum	ARRs[d]	LAT GRBs
1	1–2	494[b]	150	79	29	4	55	52	862[c]	40	38
2	3–4	466	17	183	363	0	132	59	1220	47	29
3	5–6	451[b]	9	207	399	2	90	65	1223	33	42
4	7–8	464[b]	65	215	318	173	422	82	1739	47	36
4	9–10	485	17	196	67	228	324	73	1390	53	41
4	1–10	2360[b]	258	880	1176	407	1023	331	6434	220[e]	186

Notes.
[a] The triggers of a mission year are always counted from July 12 to July 11 of the following year, starting with trigger enabling on 2008, July 12.
[b] GRB 091024A, GRB 130925A, GRB 150201A, and GRB 160625B each of which triggered GBM twice, are counted twice. Hence, the total number of GRBs is one less in mission years 1 and 2 and 5 and 6, two less in missions years 7 and 8, and four less for the 10 year sum.
[c] The total number of triggers is two less compared to Paciesas et al. (2012), since the two commanded triggers (bn100709294 and bn100711145) were not counted.
[d] Derived from the Fermi timeline posting page at FSSC: https://fermi.gsfc.nasa.gov/ssc/observations/timeline/posting/arr/.
[e] Due to misclassification of events as GRBs by the flight software (FSW), 48 of the ARRs occurred for other event types. Of these, 34 occurred due to charged particle events, 5 occurred due to SGR events, 8 occurred due to solar flare events, and 1 was due to a TGF event. In addition, there were a few positive ARRs from GBM triggers followed by no spacecraft slews, which were disabled at the spacecraft level at that time. In a few cases, the spacecraft slew started well after the GBM trigger due to Earth's limb constraint.

LAT detected an additional 10 GRBs that were independently detected by instruments other than GBM.

In addition to the standard Fermi-GBM GRB catalog products, which are the GRB location, duration, peak flux, and fluence, the first three catalogs provided supplementary information. Paciesas et al. (2012) investigated the apparent improvement in trigger sensitivity relative to BATSE, which was discussed in more detail in the second catalog (von Kienlin et al. 2014), including a comparison of the numbers of BATSE- and non-BATSE-like GBM GRB triggers. The six year catalog (Bhat et al. 2016) provided an accurate estimate of the daily burst rate and employed statistical methods to assess clustering in the GRB duration-hardness distribution. It was found that the GRBs are better fit by a two-component model with short-hard and long-soft bursts than by a model with three components.

The intention of the GBM catalogs is to provide the community a foundation upon which to perform more detailed follow-up analysis, taking advantage of the huge dataset of GBM-detected GRBs, and to act as a general reference. Numerous studies using the previous GBM catalogs have been presented elsewhere (e.g., Kovacevic et al. 2014; Aartsen et al. 2015; Charisi et al. 2015; Calderone et al. 2015; Kaneko et al. 2015; Pe'er 2015; Tarnopolski 2015; Abbott et al. 2017a; Hurley et al. 2017; Andrade et al. 2019). Furthermore, we emphasize the relevance of the GBM data for multi-messenger astrophysics, which has assumed greater importance following the first coincident detection of gravitational waves (GWs) and electromagnetic (EM) radiation from the same event, namely the binary neutron star merger event detected by Fermi-GBM and LIGO on 2017 August 17 (Abbott et al. 2017b; Goldstein et al. 2017). Following this ground-breaking discovery, a search of the GBM data for GRBs with characteristics similar to GRB 170817A was conducted for the full time period of the current catalog (von Kienlin et al. 2019). A total of 13 candidates were identified during 10 mission years, from which it is predicted that Fermi-GBM will trigger on board on about one burst similar to GRB 170817A per year.

In order to highlight the successful operation of Fermi-GBM in its first decade of operation, Section 2 summarizes the 10 year trigger statistics. The GBM instrument, its data products, and onboard triggering capabilities were discussed in detail in the instrument paper (Meegan et al. 2009) and previous catalogs. Here we provide a short recap in the introduction of Section 3 and in Section 3.1. Section 3.2 presents the instrument configuration history of the latest four years, which augments the information provided in previous catalogs. Section 3.3 introduces a new tool for advanced ground processing, enabled early in 2016, which has been shown to facilitate the daily burst advocate (BA) work. The types of official GBM GCN products (circulars and notices) routinely derived from trigger data are described in Section 3.4. The standard catalog tables are presented in Section 4 and discussed in Section 5. Finally, in Section 6, we conclude with a summary.

2. Trigger Statistics

The merit of Fermi-GBM is best shown by its trigger statistics over the full time range of the current catalog (see Table 1 and Figure 1). During its first 10 years of operations, GBM triggered 6434 times, of which 2360 triggers are classified as GRB events. The remaining triggers include events from other cosmic and terrestrial sources, as well as sources of instrumental background such as terrestrial magnetospheric activity.

In accordance with the time periods covered by the first three GBM catalogs, which were two years each, the entries of Table 1 are subdivided into two year sections. Because the fourth catalog adds a four year time period, the table lists it in two rows, covering two years each. The last row gives the full 10 year trigger statistics.

Table 1 lists, in addition to the GRB triggers, the numbers of triggers caused by other sources, such as bursts of soft gamma repeaters (SGRs) due to magnetar activity, triggers on terrestrial gamma-ray flashes (TGFs), which are connected to thunderstorm activity in the Earth's atmosphere, and triggers on solar flares (SFs). Finally, in 2015 and 2017, non-SGR bursting activity from Galactic sources triggered GBM numerous times, as reflected in the column "Galactic."

In addition to bursts of gamma-rays, GBM triggers on charged particles (CPs) interacting with the sensitive detector volume, which are typically magnetospheric events, or, more rarely, cosmic-ray showers. Magnetospheric events occur predominantly in trapped particle regions traversed in the course of Fermi's orbit, mostly in the entry or exit regions of

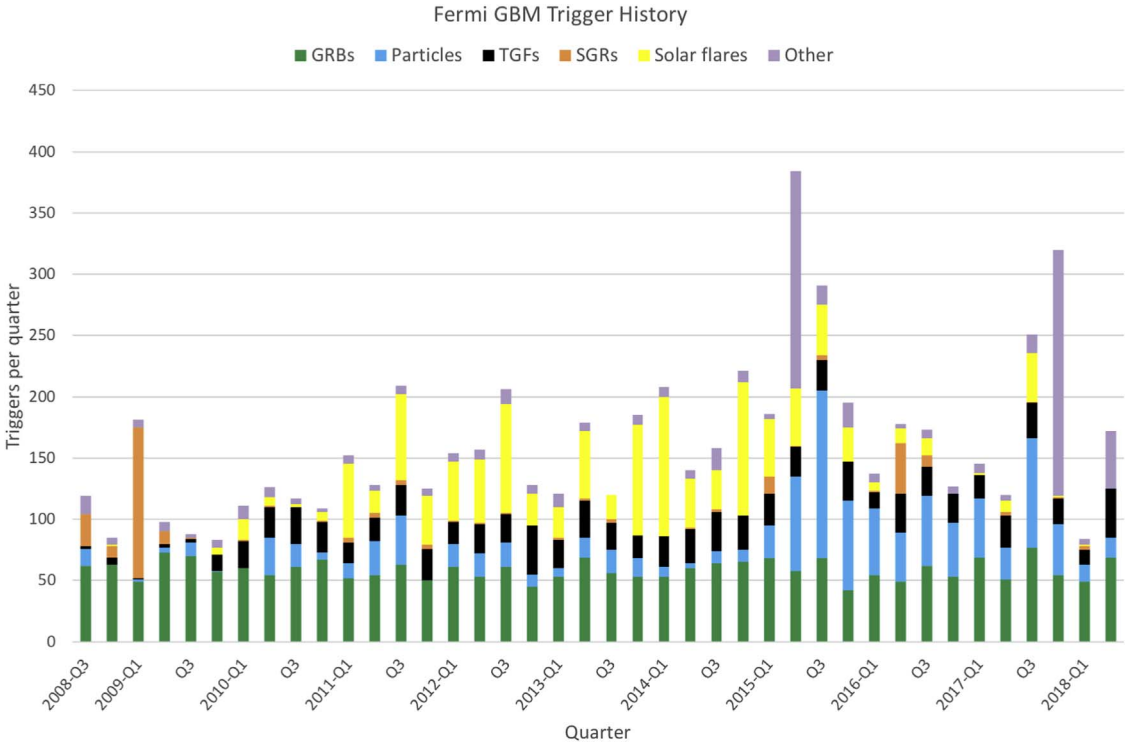

Figure 1. Quarterly trigger statistics over the first 10 years of the mission, starting from 2008 July 12 until 2018 June 30.

the South Atlantic Anomaly (SAA) or at high geomagnetic latitude. Rarely do accidental triggers happen due to background fluctuations or the observed flux is too weak for the trigger source to be identified. These extra triggers are summed in the "Other" column of Table 1.

Table 1 also lists the number of Autonomous Repoint Requests (ARRs) generated by GBM during these intervals. The ARR capability allows GBM to repoint the spacecraft in response to particularly bright triggers, thereby bringing the burst direction into the LAT FOV and/or keeping it in the LAT FOV for an extended interval. This capability has been exploited successfully for most of the mission, but it has been disabled since 2018 March 16 due to issues with a stuck spacecraft solar panel.

The quarterly trigger statistics shown in Figure 1 reflect the temporal activity variation of the different kind of sources. The increased trigger rate on solar flare events during the solar maximum period between 2011 and 2017 is obvious, as is the prolific bursting activity of several magnetars. The latter mostly coincided during the first mission year, during which the activity of three sources predominated: SGR J1550–5418 (van der Horst et al. 2012; von Kienlin et al. 2012), SGR J0501 +4516, and 1E 1841–045. A dedicated catalog summarizes the results on magnetars as observed by Fermi-GBM in the first five mission years (Collazzi et al. 2015). Non-SGR bursting activity of a few Galactic sources clearly stands out among the "Other" sources bar in the plot. These are mainly due to the bright source V404 Cyg, a black hole binary, in 2015 (2015-Q2) (Jenke et al. 2016) and to Swift J0243.6+6124 in 2017 (2017-Q4), a newly discovered Galactic Be/X-ray binary (Wilson-Hodge et al. 2018). Other triggers contributing to the "Other" sources bar are accidental triggers and triggers with uncertain source classification. A large fraction of the accidental triggers result from the algorithms that use BGO data. The significance levels of these triggers are purposely set low in order to increase the sensitivity for TGFs, which have typical durations much less than the minimum resolution (16 ms) of the data used for triggering.

An increased number of triggers on particle events is observed for the years 2015–2017, mainly by triggers during SAA entry and exit. This could be explained by expansion of the SAA beyond the predefined region stored in the GBM FSW, within which the high voltages of the GBM photomultipliers are switched off and no science data are taken, thereby disabling triggering. As expected, the quarterly rate of GRB triggers does not change significantly, fluctuating around a value of 60 triggers/quarter. The rate of triggered TGFs increased in 2009 November (2009-Q4) thanks to an update of the FSW, improving the capabilities for onboard triggering on TGFs. The actual catalog of Fermi-GBM TGFs (Roberts et al. 2018) includes, in addition, to the offline identified TGFs, a list of 686 brighter TGFs, which were able to trigger the GBM FSW, detected since launch in 2008 July 11 through 2016 July 31. This catalog is accessible online.[14]

3. Fermi-GBM: Instrument Overview and Updates

Fermi-GBM is one of two instruments on the Fermi Gamma-ray Space Telescope, which was launched on 2008 June 11. GBM is made up of two types of scintillation detectors, 12 NaI (Tl) detectors, sensitive from 8 keV to ~1 MeV, and two BGO detectors, sensitive from 200 keV to 40 MeV. The NaI(Tl) detectors are arranged in four groups of three on the corners of the spacecraft so that they view the whole unocculted sky. The BGO detectors are located on opposite sides of the spacecraft to enable an all-sky view. A detailed description of the instrument, its detectors, and electronics can be found in the GBM instrument paper (Meegan et al. 2009).

[14] Fermi-GBM TGF catalog at FSSC: https://fermi.gsfc.nasa.gov/ssc/data/access/gbm/tgf/.

3.1. GBM Onboard Triggers and Data Products

The GBM FSW continuously monitors the counting rates in each of several preset energy ranges and timescales and initiates a burst trigger when the rates in two or more detectors exceed fixed thresholds, defined in units of the standard deviation of the background rates. A detailed list of the current trigger levels is provided in Section 3.2. GBM produces triggered and continuous data types. Triggered data types, available since launch, include accelerated CTIME data (binned to 64 ms, 8 energy channels) and accelerated CSPEC data (binned to 1.024 s, 128 energy channels) for 10 minutes and Time Tagged Event data (individual events at 2 μs resolution, 128 energy channels) for 5 minutes after a trigger. The continuous data types are CTIME (256 ms, 8 energy channels) and CSPEC (4.096 s, 128 energy channels) available since launch and Continuous Time Tagged Event (CTTE) data (2 μs, 128 energy channels, available since an FSW update in 2012 November).

3.2. Instrument Configuration History

A total of 120 different trigger algorithms may be defined and operated concurrently, each with a specific combination of energy range, timescale, and threshold. Individual trigger algorithms may be disabled or enabled by telecommand. Originally, only data from the NaI(Tl) detectors could be used for triggering. However, beginning in 2009 the FSW was modified to include four additional trigger types that include data from the BGO detectors in their algorithms. Since launch the available energy ranges for triggering have not been changed. For the NaI(Tl) detectors these are, in units of keV: 25–50, 50–300, >100, and >300. For the BGO triggers the energy range from 2 to 40 MeV is used. The available trigger timescales range from 0.016 s to 8.192 s in steps of a factor of two. Except for the 0.016 s timescale, pairs of triggers on the same timescale may be offset by half of the time bin to improve the sensitivity (Band 2002). The first three GBM GRB catalog papers include the history of enabled triggers and their settings through the first six mission years.[15] Here we summarize the settings during the subsequent four mission years. Table 2 lists the enabled trigger algorithms at the start of mission year 7, along with their threshold settings, which were not altered subsequently.

The low-level threshold (LLT) values are adjustable by telecommand but are generally set at the same values for long periods of time, except for intervals of solar activity when an excessive rate of non-GRB triggers is likely.[16] Since 2012 no modification of the LLT settings has been needed because other flight software settings were used to minimize triggering by the same transient event. The practice of regularly disabling certain soft-energy triggers on weekends and US public holidays, which began in 2012 July, was continued during years 7–10. During weekend times trigger algorithms 22–26 were disabled starting from Friday 15–20 hr UT until Monday 13–20 hr UT for durations anywhere between 60 and 80 hr. Table 3 includes the trigger algorithm changes during years 7–10, except for the weekend disabling. In the interest of brevity the latter changes are listed separately online. During mission years 7–10 solar activity continued to be a significant complicating factor affecting the GBM science data. In particular, the CTTE data

[15] We have to note that the threshold values listed in Table 2 of Bhat et al. (2016) are wrong.

[16] A table summarizing the intervals of the non-nominal trigger settings is posted at https://fermi.gsfc.nasa.gov/ssc/data/access/gbm/llt_settings.html.

Table 2
Trigger Algorithms at the Start of Mission Year 7

Algorithm Number	Timescale (ms)	Offset (ms)	Channels	Energy (keV)	Threshold (0.1σ) 2014 Jul 12
1	16	0	3–4	50–300	75
2	32	0	3–4	50–300	75
3	32	16	3–4	50–300	75
4	64	0	3–4	50–300	50
5	64	32	3–4	50–300	50
6	128	0	3–4	50–300	50
7	128	64	3–4	50–300	50
8	256	0	3–4	50–300	45
9	256	128	3–4	50–300	45
10	512	0	3–4	50–300	45
11	512	256	3–4	50–300	45
12	1024	0	3–4	50–300	45
13	1024	512	3–4	50–300	45
14	2048	0	3–4	50–300	45
15	2048	1024	3–4	50–300	45
16	4096	0	3–4	50–300	45
17	4096	2048	3–4	50–300	45
18[b]	8192	0	3–4	50–300	50
19[b]	8192	4096	3–4	50–300	50
20[b]	16384	0	3–4	50–300	50
21[b]	16384	8192	3–4	50–300	50
22	16	0	2–2	25–50	80
23	32	0	2–2	25–50	80
24	32	16	2–2	25–50	80
25	64	0	2–2	25–50	55
26	64	32	2–2	25–50	55
27[b]	128	0	2–2	25–50	55
28[b]	128	64	2–2	25–50	55
29[b]	256	0	2–2	25–50	55
30[b]	256	128	2–2	25–50	55
31[b]	512	0	2–2	25–50	55
32[b]	512	256	2–2	25–50	55
33[b]	1024	0	2–2	25–50	55
34[b]	1024	512	2–2	25–50	55
35[b]	2048	0	2–2	25–50	55
36[b]	2048	1024	2–2	25–50	55
37[b]	4096	0	2–2	25–50	65
38[b]	4096	2048	2–2	25–50	65
39[b]	8192	0	2–2	25–50	65
40[b]	8192	4096	2–2	25–50	65
41[b]	16384	0	2–2	25–50	65
42[b]	16384	8192	2–2	25–50	65
43	16	0	5–7	>300	80
44[b]	32	0	5–7	>300	80
45[b]	32	16	5–7	>300	80
46[b]	64	0	5–7	>300	60
47[b]	64	32	5–7	>300	60
48[b]	128	0	5–7	>300	55
49[b]	128	64	5–7	>300	55
50	16	0	4–7	>100	80
51[b]	32	0	4–7	>100	80
52[b]	32	16	4–7	>100	80
53[b]	64	0	4–7	>100	55
54[b]	64	32	4–7	>100	55
55[b]	128	0	4–7	>100	55
56[b]	128	64	4–7	>100	55
57[b]	256	0	4–7	>100	55
58[b]	256	128	4–7	>100	55
59[b]	512	0	4–7	>100	55
60[b]	512	256	4–7	>100	55
61[b]	1024	0	4–7	>100	55
62[b]	1024	512	4–7	>100	55
63[b]	2048	0	4–7	>100	55

Table 2
(Continued)

Algorithm Number	Timescale (ms)	Offset (ms)	Channels	Energy (keV)	Threshold (0.1σ) 2014 Jul 12
64[b]	2048	1024	4–7	>100	55
65[b]	4096	0	4–7	>100	65
66[b]	4096	2048	4–7	>100	65
116[a]	16	0	5–7	>300	55
116[a]	16	0	BGO/3–6	2-40 MeV	55
117[a]	16	0	5–7	>300	45
117[a]	16	0	BGO/3–6	2-40 MeV	45
118[a]	16	0	5–7	>300	45
118[a]	16	0	BGO/3–6	2–40 MeV	45
119[a]	16	0	BGO/3–6	2-4-0 MeV	47

Notes.
[a] Trigger algorithms using the BGO detector count rates. Algorithm 116 triggers when at least 2 NaI detectors and 1 BGO detector exceed the trigger threshold. Algorithm 117 is the same as 116, but imposes the additional requirement that the triggered detectors are on the $+X$ side of the spacecraft. Algorithm 118 is the same as 117, but requires the triggered detectors to be on the $-X$ side of the spacecraft. Algorithm 119 requires a significant rate increase in both BGO detectors independently of the NaI detectors.
[b] Those algorithms have been disabled during most of the mission.

mode, which was implemented beginning in late 2012, may be interrupted or modified to mitigate excessive rates of CTTE data, usually caused by solar activity. In its normal operation this "throttling" uses FSW monitoring of a variety of data rates to interrupt CTTE data production from the Sun-facing NaI detectors (n0-n5). When more restrictive "aggressive" throttling is enabled, CTTE data production is interrupted from all 12 NaI detectors. The list below includes the periods when aggressive throttling was enabled but not the times when throttling actually occurred. Configuration changes that altered the volume and/or contents of CTTE data are also listed in Table 3. Listed below are the major configuration changes during mission years 7–10, which are also included in Table 3.

8/12/2014: the GBM onboard clock, which counts the elapsed time since 2001 January 1, experienced a rollover at 00:38:46 UT. To minimize unexpected issues with this expected occurrence, all triggers were disabled prior to the rollover. However, an unexpected impact of the rollover was a high rate of spurious triggering. All triggering was again disabled for a longer period while the issue was studied and the problem (a stale background rates buffer) was corrected.

9/11-15/2014: a further impact of the clock rollover was discovered on 9/11, when a bright solar flare produced a high rate of CTTE data that should have been throttled by the FSW. CTTE mode was disabled while the issue was studied. The cause turned out to be another stale time buffer. The problem was corrected on 9/15 by restarting continuous CTTE mode.

10/22-28/2014: invoked aggressive throttling of CTTE data.

2/23-26/2015: CTTE data mode was disabled and CTIME data accumulation set to 64 ms, due to flaring activity of SGR 1935+2154.

3/12-13/2015: long-soft trigger algorithms 25–26 were disabled; algorithms 22–24 were kept enabled.

9/29-10/5/2015: disabled all TTE data production and set CTIME data accumulations to 64 ms due to elevated solar activity. Algorithms 25–26 were disabled while keeping 22–24 enabled.

3/3/2016: BGO PMT Gain Balance Test was performed. ARRs were disabled; trigger algorithms 116–119 were disabled.

9/6-11/2017: invoked aggressive throttling of CTTE data and disabled soft triggers.

11/6-27/2017: disabled/enabled trigger algorithms 8–17.

3/16-28/2018: GBM was put in safe mode for 12 days due to a spacecraft solar panel drive anomaly.[17]

3.3. Advanced Ground Processing

Beginning in early 2016, an automated localization algorithm, called the RoboBA, was placed into operation within the GBM Burst Alert Pipeline (BAP). The RoboBA is a set of automated algorithms developed to replace the Human-in-the-Loop (HitL) localization for most GRB triggers. HitL processing requires BAs to be on call at all times and ready to promptly localize the GBM low-latency trigger data, which has faced a median 1–2 hr latency. Due to the increasing interest in and importance of GBM-detected and localized GRBs, localizations of GRBs are desirable as soon as possible. The RoboBA now provides localizations for GRBs with accuracy equivalent to the human BA processing for GRBs within 10 minutes after trigger. The RoboBA also provides a preliminary estimate in the GCN notice whether the GRB is likely to be a short or long duration GRB, with a success rate of >85% when compared to the final T_{90}. Once the RoboBA performs the localization, the BAP submits a GCN Notice and Circular for the RoboBA localization. The pipeline automatically creates the localization products, including the full-sky HEALPix map of the localization incorporating the estimated systematic uncertainty model, and uploads them to the High-Energy Astrophysics Science Archive Research Center (HEASARC). The RoboBA has a complete end-to-end automatic processing success rate of >80%, with most failures due to dropped data packets in the real-time communication stream from the spacecraft. RoboBA catches these failures and reports them to the human BA so that a manual localization can be performed. A detailed description of the RoboBA algorithm, an evaluation of its effectiveness, and the improvements implemented in the algorithm in 2019 are described in Goldstein et al. (2019).

3.4. Fermi-GBM GCN Notices and Circulars

Here we list the actual Gamma-ray burst Coordinates Network (GCN) notices and circulars relevant for GRBs as announced in 2019 (Fermi Team 2019), which are released automatically or by the GBM BA.

3.4.1. Official Fermi-GBM notices:

Notices are automated, standard format text messages designed to be easily parsed by a computer. They are typically low latency, within tens of seconds to 10 minutes of the GRB trigger, and can be found here https://gcn.gsfc.nasa.gov/fermi_grbs.html or subscribed to through GCN.

[17] One of the solar panels stuck and remained in a fixed position at least through the reporting period of this catalog. As a consequence a modified Fermi rocking strategy has been adopted. A further impact is that ARRs have been disabled since then.

Table 3
Trigger Modification History

Date	Year/DOY/UT	Operation
2014 Aug 12	2014/224:00:27:46	Disable triggers
	2014/224:00:40:00	Enable triggers
	2014/224:04:53:46	Disable triggers
	2014/224:16:29:42	Enable triggers
2014 Sep 11	2014/254:13:19:15	Disable Continuous TTE data
2014 Sep 15	2014/258:18:25:22	Re-enable Continuous TTE data
2014 Oct 22	2014/295:13:48:59	Start aggressive throttling of TTE data and Disable soft triggers
2014 Oct 28	2014/301:19:50:27	Set TTE throttling back to normal levels
2015 Feb 23	2015/054:17:51:54	Turn off Continuous TTE data because of a flaring SGR
2015 Feb 23	2015/054:17:52:24	Accelerate CTIME data accumulations intervals to 64 ms
2015 Feb 26	2015/057:17:21:38	Turn on Continuous TTE data production
2015 Feb 26	2015/057:17:22:11	Decelerate CTIME accumulations
2015 Mar 12	2015/071:14:59:58	Disable long (64 ms) soft trigger algorithms while keeping short soft algorithms enabled
2015 Sep 29	2015/272:15:48:47	Turn off all TTE data production because of elevated Solar activity.
2015 Sep 30	2015/273:14:41:58	Accelerate CTIME data accumulation intervals to 64 ms to study SGR's
2015 Oct 2	2015/275:19:29:03	Disable 64 ms soft trigger algorithms 25 and 26 while keeping short soft algorithms enabled
2015 Oct 5	2015/278:15:24:22	Turn on all TTE data production
2015 Oct 5	2015/278:18:39:02	Decelerate CTIME accumulations
2016 Mar 3	2016/063:12:20:00	Disable the BGO AGC's (Collect data for BGO PMT Gain Balance Test)
	2016/063:12:20:05	Disable ARRs
	2016/063:12:20:10	Turn off algorithms 116–119 (TGF algorithms)
	2016/063:12:20:15	Turn off PMTs 12 and 14 (BGO detectors)
	2016/063:18:00:15	Turn on PMTs 12 and 14
	2016/063:23:50:00	Turn on PMTs 13 and 15
	2016/063:23:50:05	Set ARR threshold back to McIlwain 158
	2016/063:23:50:10	Enable the BGO AGC's
	2016/063:23:50:15	Re-enable the TGF trigger algorithms (116–119)
2017 Sep 6	2017/249:19:33:33	Aggressively throttle TTE data and Disable soft triggers
2017 Sep 7	2017/250:15:37:34	Set throttling of TTE data back to normal; Re-enable the soft trigger algorithms
2017 Sep 7	2017/250:19:15:49	Aggressively throttle TTE data and Disable soft triggers
2017 Sep 7	2017/250:21:49:09	Set throttling of TTE data back to normal; Re-enable the soft trigger algorithms.
2017 Sep 8	2017/251:15:02:41	Aggressively throttle TTE data and Disable soft triggers
2017 Sep 11	2017/254:16:24:20	Set throttling of TTE data back to normal; Re-enable the soft trigger algorithms
2017 Nov 3	2017/307:22:02:48	Disable the algorithms 12–15
2017 Nov 6	2017/310:21:19:15	Disable algorithms 10–17
2017 Nov 7	2017/311:20:06:20	Disable algorithms 10–17
2017 Nov 8	2017/312:19:05:54	Disable algorithms 8–17 and 25–26
2017 Nov 15	2017/319:22:52:32	Re-enable algorithms 8 and 9
2017 Nov 21	2017/325:18:06:51	Re-enable algorithms 8 through 11
2017 Nov 27	2017/331:19:22:30	Re-enable algorithms 12 through 17
2018 Mar 16	2018/075:05:12:00	GBM Turned to safe mode
2018 Mar 28	2018/087:13:43:55	Boot GBM after safe mode
	2018/087:13:59:31	HV on
	2018/087:14:04:14	TTE on
	2018/087:14:05:56	Master start to enable triggers

Note. Table 3 is published in its entirety online. A portion is shown here for guidance regarding its form and content.

(This table is available in its entirety in machine-readable form.)

1. GBM Alert: initial alert includes trigger time, trigger significance, trigger algorithm, trigger timescale.
2. GBM Flight position: Fermi-GBM onboard calculated localization, generated onboard Fermi, tens of seconds after trigger (may be multiple notices).
3. GBM Ground position: intermediate ground localization based on the latest onboard generated GRB detector rate information (may be multiple notices).
4. GBM Final Position: reports the ground generated RoboBA or Human-in-the-Loop (BA) final localization and whether the GRB was likely long or short; 10 minutes after trigger using the full trigger dataset.
5. Fermi-GBM SubThreshold: reports the time, duration, localization, and reliability for candidate short GRBs found in ground searches of CTTE data (latency here is longer than 10 minutes). See https://gcn.gsfc.nasa.gov/fermi_gbm_subthreshold.html.

3.4.2. Official Fermi-GBM Circulars:

Circulars are reports of follow-up observations made by the observers.

Table 4
GRB Triggers: Locations and Trigger Characteristics

Trigger ID	GRB Name	Time (UT)	α (°)	δ (°)	Error (°)	Location Source	Algorithm	Timescale (ms)	Energy (keV)	Other Detections[a]
bn080714086	GRB 080714B	02:04:12.0534	41.9	8.5	7.5	Fermi-GBM	10	512	47-291	K
bn080714425	GRB 080714C	10:12:01.8376	187.5	−74.0	8.7	Fermi-GBM	17	4096	47-291	
bn080714745	GRB 080714A	17:52:54.0234	188.1	−60.2	0.0	Swift	13	1024	47-291	K, R, IA, S, Me, A
bn080715950	GRB 080715A	22:48:40.1634	214.7	9.9	2.0	Fermi-GBM	29	256	23-47	K, Me, A
bn080717543	GRB 080717A	13:02:35.2207	147.3	−70.0	4.7	Fermi-GBM	17	4096	47-291	
bn080719529	GRB 080719A	12:41:40.9578	153.2	−61.3	13.8	Fermi-GBM	16	4096	47-291	K, A
bn080720316	...	07:35:35.5476	86.2	−41.8	3.2	Fermi-GBM	0	0		
bn080723557	GRB 080723B	13:22:21.3751	176.8	−60.2	0.0	Swift	8	256	47-291	K, IA, IS, Me, A
bn080723913	GRB 080723C	21:55:23.0583	113.3	−19.7	9.9	Fermi-GBM	5	64	47-291	W
bn080723985	GRB 080723D	23:37:42.7083	105.3	71.1	1.0	Fermi-GBM	11	512	47-291	K, IA, Me, W, A

Notes. Table 4 is published in its entirety online. A portion is shown here for guidance regarding its form and content.
[a] Other instrument detections: Mo: Mars Observer , K: Konus-Wind, R: RHESSI, IA: INTEGRAL SPI–ACS, IS: INTEGRAL IBIS–ISGRI, S: Swift, Me: Messenger, W: Suzaku, A: AGILE, M: MAXI, L: Fermi LAT, Nu: NuSTAR, ARR: Autonomous Repoint Requests by GBM FSW.

(This table is available in its entirety in machine-readable form.)

Table 5
GRB Durations (50–300 keV)

Trigger ID	Detectors Used	T_{90} (s)	T_{90} start (s)	T_{50} (s)	T_{50} start (s)
bn080714086	3+4+8	5.376 ± 2.360	−0.768	2.816 ± 0.810	−0.256
bn080714425	0+9+10	40.192 ± 1.145	−4.352	11.776 ± 1.619	−1.280
bn080714745	5	59.649 ± 11.276	−0.512	25.088 ± 7.940	2.560
bn080715950	0+1+2+9+10	7.872 ± 0.272	0.128	6.144 ± 0.264	1.088
bn080717543	2+10	36.609 ± 2.985	−5.376	13.056 ± 0.810	1.024
bn080719529	6+7+9	16.128 ± 17.887	−4.352	8.448 ± 1.280	−2.048
bn080720316[a]	6+7+9	16.128 ± 17.887	−4.352	8.448 ± 1.280	−2.048
bn080723557	4	58.369 ± 1.985	2.368	40.513 ± 0.231	14.208
bn080723913	0+1+3	0.192 ± 0.345	−0.064	0.064 ± 0.143	−0.064
bn080723985	2+5	42.817 ± 0.659	3.072	25.280 ± 0.405	12.160

Notes. Table 5 is published in its entirety online. A portion is shown here for guidance regarding its form and content.
[a] Data problems precluded duration analysis.

(This table is available in its entirety in machine-readable form.)

1. GRB YYMMDDX: Fermi-GBM Final Real-time Localization. Introduced in 2019 July. Automated circulars reporting the final real-time localization and HEALPix map based on our automatic processing (RoboBA, operational since early 2016). These circulars are issued for all GRBs that RoboBA localizes and include initial information about the burst duration (likely SHORT/LONG).
2. GRB YYMMDDX: Fermi-GBM Detection (RoboBA or Human-in-the-Loop generated Final localization, spectral analysis, and burst duration)
3. GRB YYMMDDX: Fermi-GBM Observation (spectral analysis, and burst duration for GRBs better localized by another instrument)

4. GRB Catalog Tables

Here we present the standard catalog tables, listing in Table 4 all 2360 triggers of the first decade of GBM operation that were classified as GRBs.[18] The associated catalog analysis results for each trigger are shown in Table 5 for the duration analysis and in Tables 6 and 7 for the peak flux and fluence analysis in two energy ranges. The GRB catalog compilation and analysis process has not changed since the production of the latest GRB catalog, and is described in detail in previous catalog papers. The standard tables of the newest catalogs always include the GRB entries of the previous catalogs, with only some minor updates for some individual GRBs, where a reanalysis was necessary. There are two browsable catalogs accessible online at HEASARC, FERMIGTRIG,[19] and FERMIGBRST.[20] All GBM triggers are entered in FERMIGTRIG, but only those triggers classified as bursts are entered in the FERMIGBRST catalog. Thus, a burst will be listed twice, once in FERMIGTRIG and once in FERMIGBRST. The burst catalog analysis requires human intervention; therefore, GRBs will be entered in the trigger catalog before the burst catalog. The latency requirements are one day for triggers and three days for bursts.

4.1. GRB Localizations and Trigger Characteristics

The catalog analysis is based on using the most reliable source locations for the determination of the instrument

[18] The total number of GBM-detected GRBs is four less, since GBM triggered twice on each of four GRBs.

[19] Fermi-GBM trigger catalog at HEASARC: https://heasarc.gsfc.nasa.gov/W3Browse/fermi/fermigtrig.html.

[20] Fermi-GBM burst catalog at HEASARC: https://heasarc.gsfc.nasa.gov/W3Browse/fermi/fermigbrst.html.

Table 6
GRB Fluence and Peak Flux (10–1000 keV)

Trigger ID	Fluence (erg cm^{-2})	PF64 (ph cm^{-2} s^{-1})	PF256 (ph cm^{-2} s^{-1})	PF1024 (ph cm^{-2} s^{-1})
bn080714086	6.76E-07 ± 4.07E-08	3.82 ± 1.06	2.24 ± 0.36	1.54 ± 0.18
bn080714425	1.81E-06 ± 2.09E-08	4.00 ± 1.45	2.96 ± 0.46	2.02 ± 0.21
bn080714745	6.33E-06 ± 1.41E-07	8.89 ± 1.61	7.78 ± 0.83	6.93 ± 0.39
bn080715950	5.04E-06 ± 7.95E-08	19.42 ± 0.95	13.58 ± 0.45	9.91 ± 0.22
bn080717543	4.46E-06 ± 7.68E-08	6.24 ± 1.08	3.43 ± 0.49	2.89 ± 0.23
bn080719529	7.75E-07 ± 2.93E-08	2.77 ± 0.83	1.77 ± 0.29	1.12 ± 0.16
bn080720316	7.75E-07 ± 2.93E-08	2.77 ± 0.83	1.77 ± 0.29	1.12 ± 0.16
bn080723557	7.22E-05 ± 2.54E-07	40.97 ± 2.24	38.24 ± 1.09	30.45 ± 0.49
bn080723913	1.34E-07 ± 1.36E-08	5.26 ± 0.70	4.13 ± 0.32	1.41 ± 0.13
bn080723985	3.08E-05 ± 2.07E-07	13.45 ± 1.24	11.36 ± 0.60	10.12 ± 0.28

Note. Table 6 is published in its entirety online. A portion is shown here for guidance regarding its form and content.
(This table is available in its entirety in machine-readable form.)

Table 7
GRB Fluence and Peak Flux (50–300 keV)

Trigger ID	Fluence (erg cm^{-2})	PF64 (ph cm^{-2} s^{-1})	PF256 (ph cm^{-2} s^{-1})	PF1024 (ph cm^{-2} s^{-1})
bn080714086	3.54E-07 ± 1.73E-08	1.52 ± 0.74	0.91 ± 0.36	0.43 ± 0.18
bn080714425	9.79E-07 ± 1.36E-08	1.03 ± 0.45	0.71 ± 0.19	0.46 ± 0.08
bn080714745	3.26E-06 ± 6.03E-08	4.41 ± 1.66	3.27 ± 0.71	2.82 ± 0.36
bn080715950	2.54E-06 ± 3.52E-08	10.70 ± 0.95	6.61 ± 0.45	3.83 ± 0.22
bn080717543	2.37E-06 ± 4.51E-08	2.14 ± 1.03	1.30 ± 0.47	1.05 ± 0.23
bn080719529	3.88E-07 ± 1.47E-08	0.59 ± 0.18	0.32 ± 0.08	0.23 ± 0.04
bn080720316	3.88E-07 ± 1.47E-08	0.59 ± 0.18	0.32 ± 0.08	0.23 ± 0.04
bn080723557	3.92E-05 ± 1.15E-07	21.19 ± 1.79	19.81 ± 1.09	15.14 ± 0.48
bn080723913	7.45E-08 ± 5.19E-09	2.62 ± 0.66	2.14 ± 0.32	0.69 ± 0.13
bn080723985	1.57E-05 ± 1.07E-07	5.92 ± 1.23	5.17 ± 0.54	4.85 ± 0.28

Note. Table 7 is published in its entirety online. A portion is shown here for guidance regarding its form and content.
(This table is available in its entirety in machine-readable form.)

response (Detecor Response Matrix). This is quite important since all of the analysis results depend on the response files generated for the particular GRB location. These locations are listed in Table 4 and are adopted from the BA (HitL) and RoboBA analysis results, which were uploaded to the GBM trigger catalog at the GIOC (with a copy at HEASARC[21]). The GBM location uncertainties shown in the table are the circular area equivalent of the statistical uncertainty (68% confidence level). There is additionally a systematic error that we have characterized for HitL localizations as a core-plus-tail model, with 90% of GRBs having a 3.7 deg error and a small tail suffering a larger than 10 deg systematic error (Connaughton et al. 2015). An evaluation of automated Fermi-GBM localizations is presented in Goldstein et al. (2019), showing that the latest version of RoboBA yields significant improvement in the systematic uncertainty, removing the long tail identified in the systematic, and improves the overall accuracy. The systematic uncertainty for the updated RoboBA localizations is 1.8 deg for 52% of GRBs and 4.1 deg for the remaining 48%. Probability maps reflecting the total uncertainty on a GBM GRB location, which are the convolution of the statistical uncertainty with the best current model for the systematic errors have been routinely delivered to the HEASARC since 2014 January, and have also been processed and delivered for the GRBs prior to 2014. An example localization contour map for GRB 170208C in shown in Figure 2.

Non-GBM locations are listed for bursts that were detected by an instrument providing a better location accuracy such as LAT, the Swift Burst Alert Telescope (BAT; Barthelmy et al. 2005) or X-ray Telescope (XRT; Burrows et al. 2005), INTEGRAL (Mereghetti et al. 2003), or were localized more precisely by the Inter-Planetary Network (Hurley et al. 2013). The higher-accuracy location source is listed under the column "Location Source," which lists only the name of the mission rather than the specific instrument on board that mission (e.g., Swift implies the locations are either from Swift-BAT or Swift-XRT or Swift-UVOT). The errors on the GRB locations determined by other instruments are not necessarily 1σ values. For the GBM analysis, a location accuracy better than a few tenths of a degree provides no added benefit because of significant systematic errors in GBM location.

The first column of Table 4 lists the GBM Trigger ID along with a conventional GRB name in the second column as defined by the GRB-observing community.[22] For years 5–10, only GBM-triggered GRBs for which a GCN Circular was issued are assigned a GRB name.

[21] https://heasarc.gsfc.nasa.gov/FTP/fermi/data/gbm/bursts/

[22] Note that the entire table is consistent with the small change in the GRB naming convention that became effective on 2010 January 1 (Barthelmy et al. 2009): if for a given date no burst has been "published" previously, then the first burst of the day observed by GBM includes the "A" designation even if it is the only one for that day.

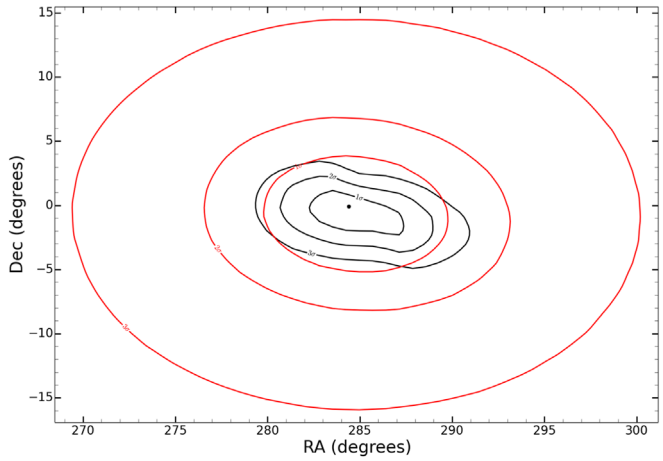

Figure 2. Probability map showing the statistical (black contours) and systematic (red contours) uncertainties of the GRB 170208C localization.

The criterion for issuing a GBM Detection/Observation Circular is if a GRB was either detected by any other mission (as listed in the last column of Table 4) or if it generated an ARR to the Fermi spacecraft or the count rate in the 50–300 keV energy range summed over the triggered detectors exceeded 1000 counts per second above the background. This arbitrary number was chosen at the beginning of the mission to focus on brighter events and not to issue too many circulars. During the 10 year period of the catalog for about 1/3 of the GRBs Fermi-GBM Detection/Observation Circulars were released.

The third column lists the trigger time in universal time (UT). Table 4 also shows which algorithm was triggered, along with its timescale and energy range. Note that the listed algorithm is the first one to exceed its threshold but it may not be the only one. The table also lists other instruments that detected the same GRB.[23] Finally, we identify the GBM GRBs for which an ARR was issued by the GBM FSW in the last column of Table 4. A total of 172 GRBs (7.3% of the total) were followed by ARRs during the first nine years of Fermi, although the spacecraft might not have slewed in every case for technical reasons, such as Earth limb constraints. The majority of these ARRs were due to high peak fluxes. In addition, there were 48 ARRs that were issued for non-GRB triggers because of misclassification by the GBM FSW.

4.2. GRB Duration, Peak Flux, and Fluence

The analysis performed to derive the duration, peak flux and fluence of each burst (as listed in Tables 5–7) is based on an automatic batch fit routine implemented within the RMFIT software.[24] It uses a forward-folding technique to obtain the best-fit parameters for a chosen model given user-selected source and background time intervals in the 10–1000 keV energy range from data files containing observed count rates and a corresponding detector response matrix. Burst durations T_{50} (T_{90}) are determined from the interval between the times where the burst has reached 25% (5%) and 75% (95%) of its maximum fluence. The burst durations T_{50} and T_{90} listed in Table 5 were computed in the 50–300 keV energy range. This is primarily due to the fact that GRBs have their maximum spectral density in this energy range. In addition, this energy range makes it easier to compare the present results with those of the predecessor BATSE. In addition the table provides the respective 1σ error estimates (Koshut et al. 1996) and start times relative to the trigger time. For a few GRBs, the duration analysis could not be performed either because the event was too weak or due to technical problems with the input data. Also, it may be noted that the duration estimates are only valid for the portion of the burst that is visible in GBM light curves summed over those NaI(Tl) detectors whose normals make less than 60° to the source. If the burst was partially occulted by Earth or had significant emission while GBM detectors were turned off in the SAA region, then the "true" durations may be underestimated or are not reliable, depending on the intensity and variability of the undetected burst emission. GRBs that triggered while Fermi was close to SAA or where the trigger is unusual in any other way, are indicated in Tables 4 and 5 by a footnote.

For technical reasons, it was not possible to perform a single analysis of the unusually long GRB 091024A (Gruber et al. 2011), GRB 130925A, and GRB 150201A, so the analysis was carried out separately for the two triggered episodes. Similarly, GRB130925A also had three emission episodes well separated in time, for which GBM triggered on the first two episodes. These cases are also noted in Tables 4 and 5. The reader may note that for most GRBs, the present analysis used data binned no finer than 64 ms, so the duration estimates (but not the errors) are quantized in units of 64 ms. However, for extremely short events, TTE/CTTE data were binned with widths of 32 ms, 16 ms, or even 8 ms in about 4% of the cases, which was necessary in order to resolve the GRBs.

As a part of the duration analysis, peak fluxes and fluences were computed in two different energy ranges. Table 6 shows the values in 10–1000 keV and Table 7 shows the values in 50–300 keV. The analysis results for low fluence events are subject to large systematic errors primarily because they use 8-channel spectral data and should be used with caution. The fluence measurements in the accompanying spectroscopy catalog (S. Poolakkil et al. 2020, in preparation), which uses the 128-channel CSPEC or TTE data, are more reliable for such weak events. The peak fluxes for each burst were computed in the same energy ranges and for three different timescales: 64, 256, and 1024 ms. Since only 20% of the bursts have detectable emission in the BGO detectors,[25] only NaI detector data were used for the catalog analysis.

5. Discussion

Here we provide the standard set of figures as shown in the previous catalogs. The sky distribution of GBM-triggered GRBs in celestial coordinates is shown in Figure 3, still reflecting now for the large 10 yr sample that both the long

[23] This information was drawn from the GCN archive accessible at http://gcn.gsfc.nasa.gov/gcn3_archive.html. A more complete list of detections is available at http://www.ssl.berkeley.edu/ipn3/masterli.txt.

[24] The spectral analysis package RMfit was originally developed for time-resolved analysis of BATSE GRB data but has been adapted for GBM and other instruments with suitable FITS data formats. The software is available at the Fermi Science Support Center: https://fermi.gsfc.nasa.gov/ssc/data/p7rep/analysis/rmfit/.

[25] GRBs with significant emission in at least one BGO detector above 300 keV were highlighted in the main GRB tables of the first two catalogs (Paciesas et al. 2012; von Kienlin et al. 2014). In the first four years there were 204 BGO bright GRBs out of 954 GRBs.

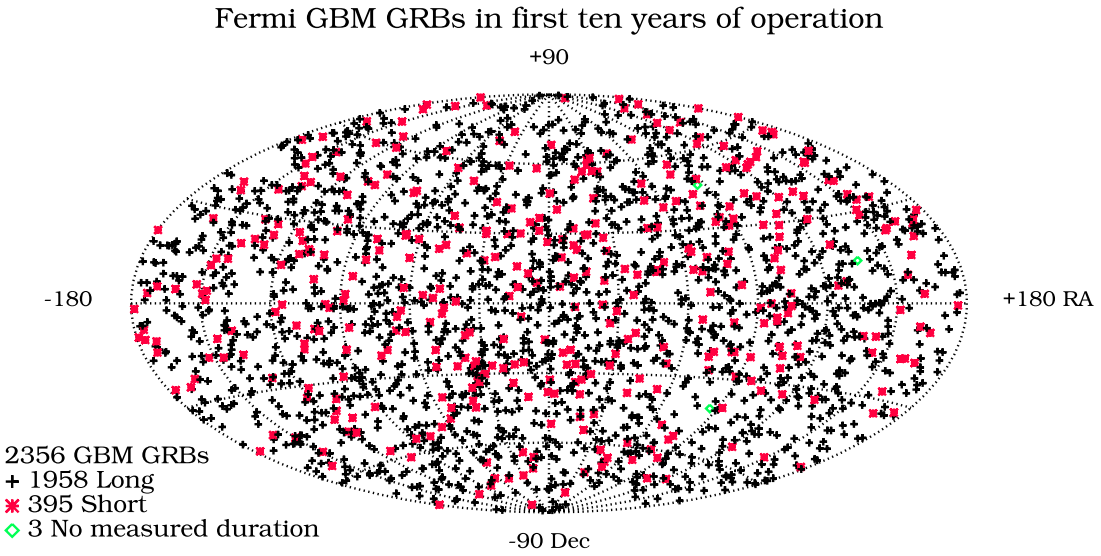

Figure 3. Sky distribution of GBM-triggered GRBs in celestial coordinates. Crosses indicate long GRBs ($T_{90} > 2$ s); asterisks indicate short GRBs.

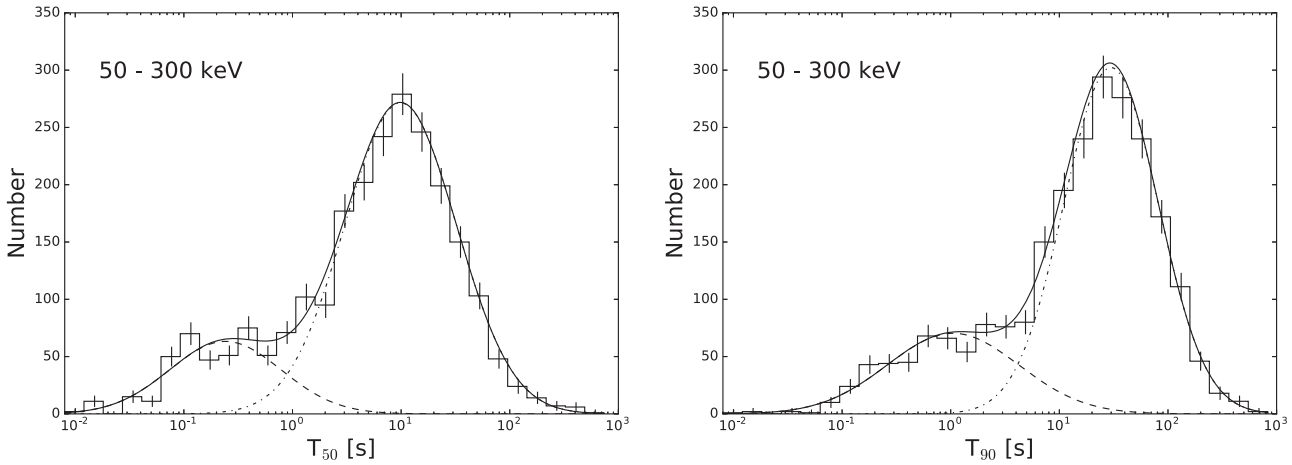

Figure 4. T_{50} (left) and T_{90} (right) distributions. Lines show the best-fitting models.

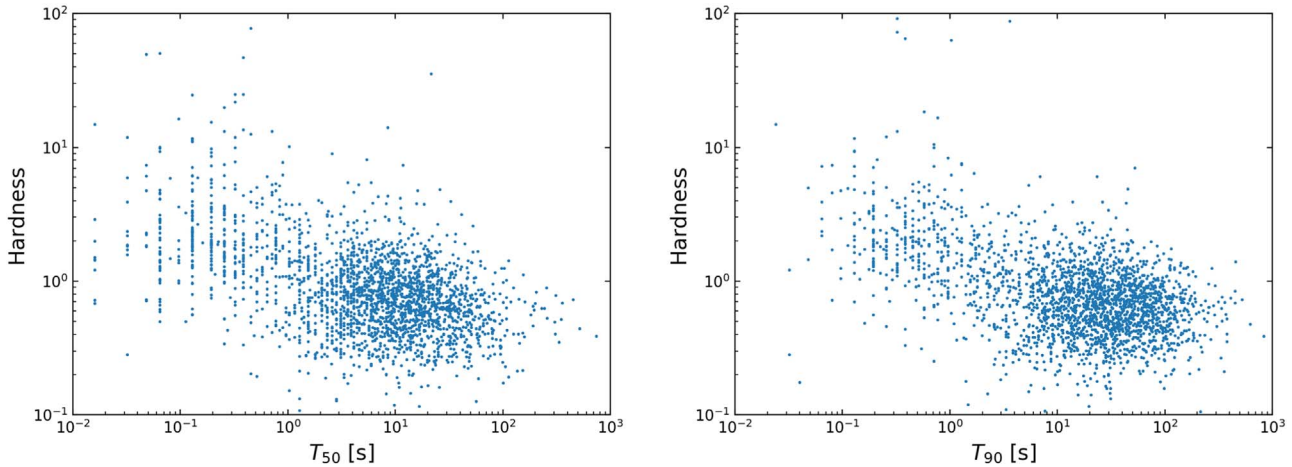

Figure 5. Scatter plots of spectral hardness vs. duration are shown for the two duration measures T_{50} (left plot) and T_{90} (right plot). The estimated errors for both quantities are not shown but can be quite large for the weak events. Nevertheless, the anti-correlation of spectral hardness with burst duration is evident.

and short GRB locations do not show any obvious anisotropy, which is consistent with an isotropic distribution of GRB arrival directions. The histograms of the logarithms of GBM-triggered GRB durations (T_{50} and T_{90}) are shown in Figure 4. Using the conventional division between the short and long GRB classes ($T_{90} \leqslant 2$ s and $T_{90} > 2$ s, respectively), we find

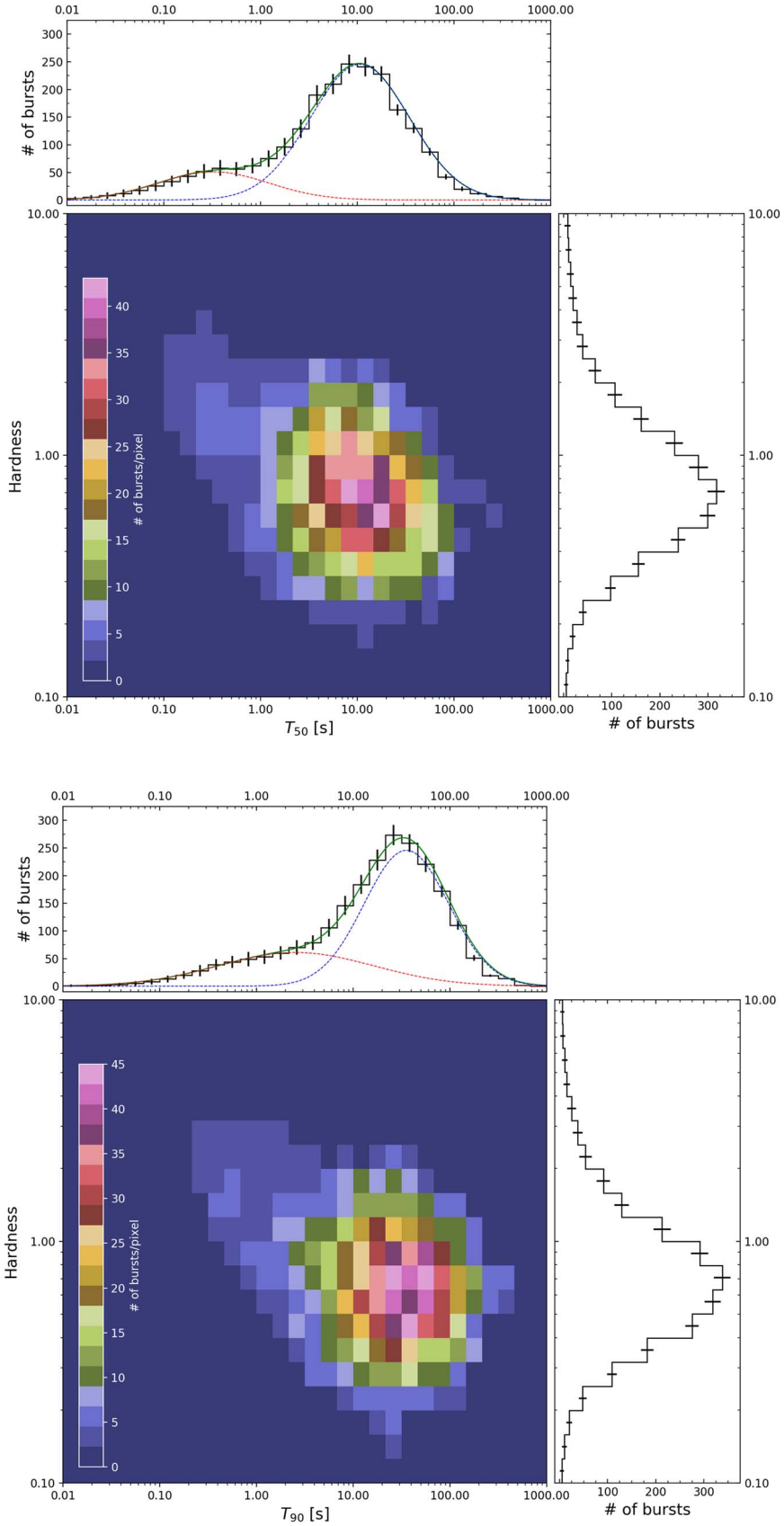

Figure 6. Two-dimensional histogrammed probability density plots of the spectral hardness vs. duration (top: T_{50}, bottom: T_{90}) accounting for the uncertainties of both parameters. The color bar provides the color mapping for the number of bursts per pixel. The plots attached to the top and right are the projections of the individual histogrammed probability densities of duration and hardness. Lognormal bimodal fits (green line) together with individual lognormal fits to the long (blue line) and short (red line) GRB classes are overplotted in the duration histograms.

Table 8
Parameters of the Gaussian Distributions for log (T_{50}) and log (T_{90})

	μ (short)	σ (short)	w (short)	μ (long)	σ (long)	w (long)
T_{50}	−0.618 (→0.241 s)	0.265	0.189	0.995 (→9.89 s)	0.265	0.811
T_{90}	0.0208 (→1.05 s)	0.367	0.245	1.476 (→29.9 s)	0.189	0.755

Note. We display the actual mean duration in parentheses ($=10^{\mu}$). Note that for the T_{50} distribution the fitting procedure yields a solution where the variances of the two components are equal, thus reducing the number of degrees of freedom.

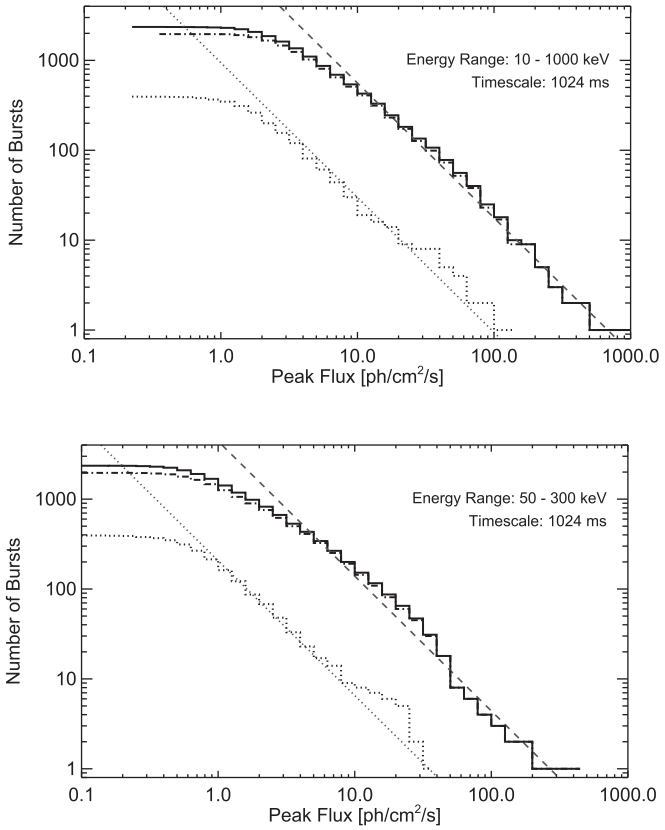

Figure 7. Integral distribution of GRB peak flux on the 1.024 s timescale. Energy ranges are 10–1000 keV (upper plot) and 50–300 keV (lower plot). Distributions are shown for the total sample (solid histogram), short GRBs (dots), and long GRBs (dash-dots), using $T_{90} = 2$ s as the distinguishing criterion. In each plot a power law with a slope of $-3/2$ (dashed line) is drawn to guide the eye.

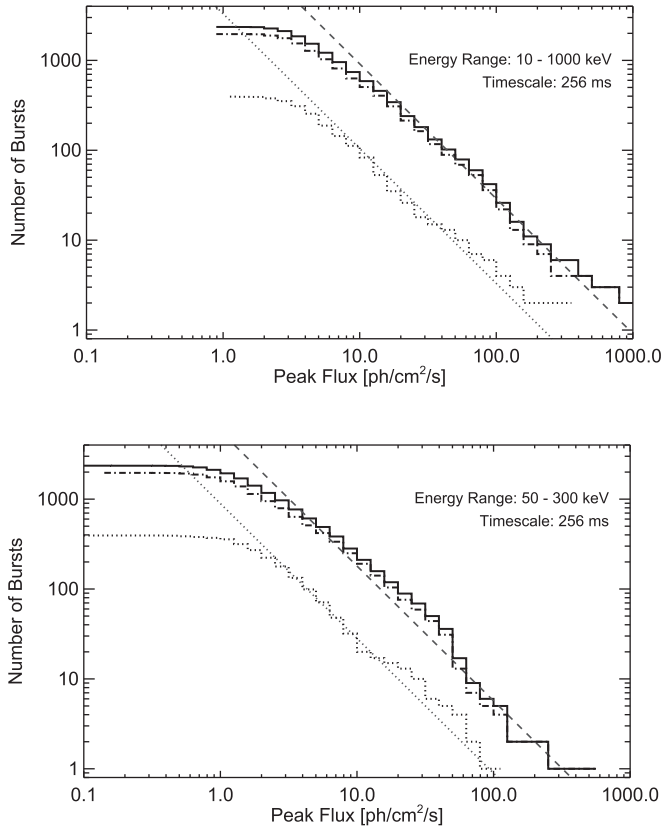

Figure 8. Same as Figure 7, except on the 0.256 s timescale.

that during the first 10 years there were 395 (17%) short GRBs and 1958 (83%) long GRBs.[26]

We fit the duration distributions using the unbinned, maximum likelihood method, Mclust (Fraley & Raftery 2002). This method assumes the components have lognormal distribution and decides the optimal number of groups using a Bayesian Information Criterion. We find both of the duration distributions are best described by a two-component model corresponding to the short and long GRB categories (see Figure 4), which reaffirms the study of Bhat et al. (2016) that did not provide any clue for an extra class, like soft-intermediate duration GRBs bridging the other two groups. The results of the fits are presented in Table 8: $N(\mu, \sigma, w)$ is a single Gaussian for the log (T_{50}) or log (T_{90}) distribution, where μ represents the mean, σ is the standard deviation, and w is the weight of the component.

[26] For three GRBs the duration measurement using our standard method was not possible.

We fit the hardness-duration distributions with the same method, and find that the best-fitting solutions are not meaningful. Namely, the algorithm finds three components: one that can be associated with the short group, and two other groups that divide the long population essentially along a constant duration with approximately equal weights. This structure does not correspond to previous studies that find three groups (Horváth et al. 2006; Veres et al. 2010). However, it might point to an asymmetric distribution (Tarnopolski 2019).

Checking in Figure 4 for the T_{90} duration at which the lognormal fits to the short and long GRB classes intersects, indicating a 50% probability that a GRB is in fact long/short we derive a T_{90} value of 4.2 s. Using this value as division of the short/long GRB populations we get 532 (22.5%) short and 1821 (77.5%) long GRBs.

Figure 5 shows scatter plots of the spectral hardness versus T_{50}- and T_{90}- durations. The spectral hardness is obtained from spectral fits for each GRB, using the photon model fit parameters, which are a byproduct of the duration analysis. By summing the deconvolved counts in each detector and time bin in two energy bands (10–50 keV and 50–300 keV), and further summing each quantity in time over the T_{50} and T_{90} intervals, the hardness was calculated

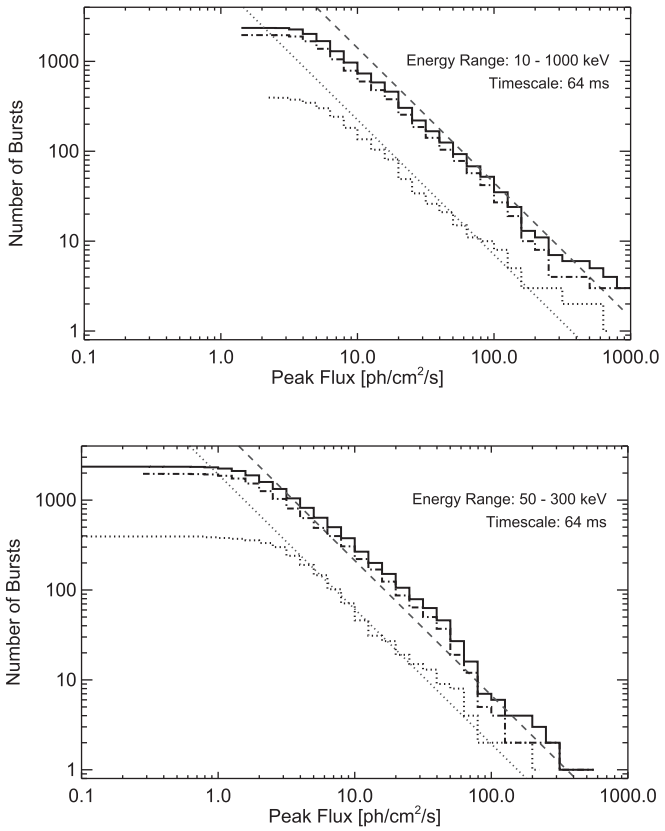

Figure 9. Same as Figure 7, except on the 0.064 s timescale.

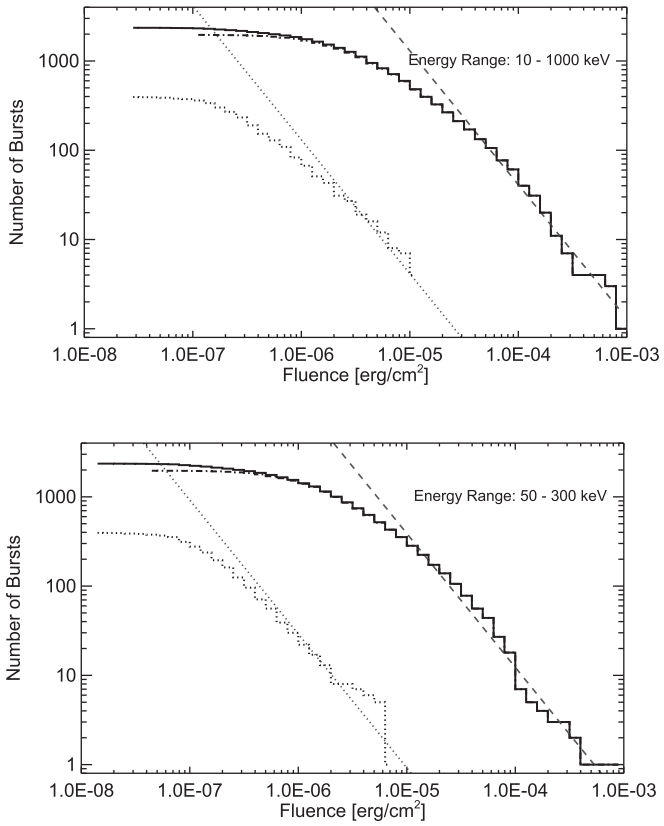

Figure 10. Integral distribution of GRB fluence in two energy ranges: 10–1000 keV (upper plot) and 50–300 keV (lower plot). Distributions are shown for the total sample (solid histogram), short GRBs (dots), and long GRBs (dash-dots), using $T_{90} = 2$ s as the distinguishing criterion. In each plot a power law with a slope of $-3/2$ (dashed line) is drawn to guide the eye.

separately for each detector as the ratio of the flux density in 50–300 keV to that in 10–50 keV, and finally averaged over detectors.

The estimated errors derived from the duration and hardness analysis are not included in the duration distributions and scatter plots shown in Figures 4 and 5. A more realistic representation of these parameters incorporating the uncertainty is shown in Figure 6 as a histogrammed probability density plot. It was derived via Monte Carlo sampling from the probability density function (PDF) of the duration and hardness parameters and their standard deviations for each GRB (Goldstein et al. 2016, S. Poolakkil et al. 2020, in preparation). By randomly selecting a value from each of those PDFs, sorting them into duration/hardness histograms with predefined bins, and additionally into pixels of the corresponding hardness-duration plane, then repeating the procedure for a number of iterations (typically >1000), we were able to derive PDFs for each histogram bin and map pixel. We choose the median as the centroid of the frequency value of each bin/pixel and the error bars shown in the duration and hardness histograms represent the 68% credible interval centered at the median.

The bimodal shape of the duration distributions shown in Figure 6 is less distinct compared to the representation of the duration distributions shown in Figure 4. Again assigning GRBs to the short/long GRB classes by using the intersection of the two lognormal fits, we obtain a value for T_{90} of 6.1 s, which is approximately 1.5 times the value derived from Figure 4, now yielding 615 (26%) in the short and 1738 (74%) in the long GRB class.

It emerges that the representation of the duration distributions as histogrammed probability density plots suggests an increased number of GBM GRBs that could be attributed to the short GRB class. This supports the result of the search for GBM GRBs similar to GRB 170817A, presented in von Kienlin et al. (2019), which already revealed candidate short GRBs with a T_{90} duration up to 3.3 ± 2.1 s.

Integral distributions of the peak fluxes observed for GRBs in the first decade are shown in Figure 7 for a 1.024 s timescale and in Figures 8 and 9 for the shorter 0.256 s and 0.064 s timescales, each separately for short and long GRBs. The conclusions drawn in previous catalogs regarding the shape of the integral distributions are strengthened. For long GRBs the deviation from the $-3/2$ power law, expected for spatially homogeneous GRBs in Euclidean space, occurs well above the GBM threshold at a flux value of $\sim$10 ph cm^{-2} s^{-1}. For short events the GBM data appear consistent with a homogeneous spatial distribution down to peak flux values around 1 ph cm^{-2} s^{-1} (50–300 keV), below which instrument threshold effects become dominant. The integral fluence distributions for the two energy intervals are shown in Figure 10.

6. Summary

The fourth Fermi-GBM Gamma-Ray Burst Catalog comprises a list of 2356 cosmic GRBs that triggered GBM between 2008 July 12 and 2018 July 11. It provides actualized tables and standard analysis results of the full 10 year sample of GBM-triggered GRBs and continues the reporting on exceptional instrument operation conditions; as such it serves as a standard database and reference for catalog-based follow-up analysis.

Standard representations of the catalog quantities and analysis results such as the sky distribution of GBM-triggered GRBs locations, the histograms of GRB T_{90}- and T_{50}–duration's and the integral distributions of GRB peak fluxes and fluences now resemble the known characteristics for the now large sample. However, for the presentation of the GRB duration versus hardness and the hardness distribution itself a more realistic presentation including the parameter uncertainties was introduced. This representation shows a less clear separation of the two most commonly anticipated constituents, the short and long GRB classes. It suggests that about a quarter of the whole GBM GRB sample is due to short GRBs, which is significantly larger compared to the fraction derived when applying the conventional division at 2 s (17 % short GRBs).

Support for the German contribution to GBM was provided by the Bundesministerium für Bildung und Forschung (BMBF) via the Deutsches Zentrum für Luft und Raumfahrt (DLR) under grant No. 50 QV 0301. The USRA coauthors gratefully acknowledge NASA funding through contract NNM13AA43C. The UAH coauthors gratefully acknowledge NASA funding from cooperative agreement NNM11AA01A. E.B. and C.M. are supported by an appointment to the NASA Postdoctoral Program, administered by the Universities Space Research Association under contract with NASA. D.K., C.A.W.H., and C.M.H. gratefully acknowledge NASA funding through the Fermi-GBM project.

ORCID iDs

A. von Kienlin https://orcid.org/0000-0002-0221-5916
W. S. Paciesas https://orcid.org/0000-0002-2481-5947
P. N. Bhat https://orcid.org/0000-0001-7916-2923
E. Bissaldi https://orcid.org/0000-0001-9935-8106
A. Goldstein https://orcid.org/0000-0002-0587-7042
C. M. Hui https://orcid.org/0000-0002-0468-6025
C. Malacaria https://orcid.org/0000-0002-0380-0041
S. Poolakkil https://orcid.org/0000-0002-6269-0452
R. D. Preece https://orcid.org/0000-0003-1626-7335
O. J. Roberts https://orcid.org/0000-0002-7150-9061
P. Veres https://orcid.org/0000-0002-2149-9846
C. A. Wilson-Hodge https://orcid.org/0000-0002-8585-0084

References

Aartsen, M. G., Ackermann, M., Adams, J., et al. 2015, ApJL, 805, L5
Abbott, B. P., Abbott, R., Abbott, T. D., et al. 2017a, ApJ, 841, 89
Abbott, B. P., Abbott, R., Abbott, T. D., et al. 2017b, ApJL, 848, L13
Ajello, M., Arimoto, M., Axelsson, M., et al. 2019, ApJ, 878, 52
Andrade, U., Bengaly, C. A. P., Alcaniz, J. S., & Capozziello, S. 2019, MNRAS, 490, 4481
Band, D. L. 2002, ApJ, 578, 806
Barthelmy, S. D., Barbier, L. M., Cummings, J. R., et al. 2005, SSRv, 120, 143
Barthelmy, S. D., Gehrels, N., Paciesas, W., et al. 2009, GCN, 10251, 1
Bhat, P. N., Meegan, C. A., von Kienlin, A., et al. 2016, ApJS, 223, 28
Burrows, D. N., Hill, J. E., Nousek, J. A., et al. 2005, SSRv, 120, 165
Calderone, G., Ghirlanda, G., Ghisellini, G., et al. 2015, MNRAS, 448, 403
Charisi, M., Márka, S., & Bartos, I. 2015, MNRAS, 448, 2624
Collazzi, A. C., Kouveliotou, C., van der Horst, A. J., et al. 2015, ApJS, 218, 11
Connaughton, V., Briggs, M. S., Goldstein, A., et al. 2015, ApJS, 216, 32
Fermi Team 2019, GCN, 24408, 1
Fraley, C., & Raftery, A. E. 2002, Journal of the American Statistical Association, 97, 611
Goldstein, A., Burgess, J. M., Preece, R. D., et al. 2012, ApJS, 199, 19
Goldstein, A., Connaughton, V., Briggs, M. S., & Burns, E. 2016, ApJ, 818, 18
Goldstein, A., Fletcher, C., Veres, P., et al. 2019, arXiv:1909.03006
Goldstein, A., Veres, c., Burns, E., et al. 2017, ApJL, 848, L14
Gruber, D., Goldstein, A., Weller von Ahlefeld, V., et al. 2014, ApJS, 211, 12
Gruber, D., Krühler, T., Foley, S., et al. 2011, A&A, 528, A15
Horváth, I., Balázs, L. G., Bagoly, Z., Ryde, F., & Mészáros, A. 2006, A&A, 447, 23
Hurley, K., Aptekar, R. L., Golenetskii, S. V., et al. 2017, ApJS, 229, 31
Hurley, K., Pal'shin, V. D., Aptekar, R. L., et al. 2013, ApJS, 207, 39
Jenke, P. A., Wilson-Hodge, C. A., Homan, J., et al. 2016, ApJ, 826, 37
Kaneko, Y., Bostancı, Z. F., Göğüş, E., & Lin, L. 2015, MNRAS, 452, 824
Koshut, T. M., Paciesas, W. S., Kouveliotou, C., et al. 1996, ApJ, 463, 570
Kovacevic, M., Izzo, L., Wang, Y., et al. 2014, A&A, 569, A108
Meegan, C., Lichti, G., Bhat, P. N., et al. 2009, ApJ, 702, 791
Mereghetti, S., Götz, D., Borkowski, J., Walter, R., & Pedersen, H. 2003, A&A, 411, L291
Paciesas, W. S., Meegan, C. A., von Kienlin, A., et al. 2012, ApJS, 199, 18
Pe'er, A. 2015, AdAst, 2015, 907321
Roberts, O. J., Fitzpatrick, G., Stanbro, M., et al. 2018, JGRA, 123, 4381
Tarnopolski, M. 2015, A&A, 581, A29
Tarnopolski, M. 2019, ApJ, 870, 105
van der Horst, A. J., Kouveliotou, C., Gorgone, N. M., et al. 2012, ApJ, 749, 122
Veres, P., Bagoly, Z., Horváth, I., Mészáros, A., & Balázs, L. G. 2010, ApJ, 725, 1955
von Kienlin, A., Gruber, D., Kouveliotou, C., et al. 2012, ApJ, 755, 150
von Kienlin, A., Meegan, C. A., Paciesas, W. S., et al. 2014, ApJS, 211, 13
von Kienlin, A., Veres, P., Roberts, O. J., et al. 2019, ApJ, 876, 89
Wilson-Hodge, C. A., Malacaria, C., Jenke, P. A., et al. 2018, ApJ, 863, 9
Yu, H.-F., Preece, R. D., Greiner, J., et al. 2016, A&A, 588, A135